Thermal excitation-energy deposition in 5–15 GeV/c hadron-induced reactions with ^{197}Au. I. Reconstruction of thermal source properties

T. Lefort,* L. Beaulieu,† K. Kwiatkowski,‡ W.-c. Hsi,§ and V. E. Viola
Department of Chemistry and IUCF, Indiana University, Bloomington, Indiana 47405

R. Laforest,‖ E. Martin, E. Ramakrishnan,¶ D. Rowland,** A. Ruangma, E. Winchester, and S. J. Yennello
Department of Chemistry and Cyclotron Laboratory, Texas A & M University, College Station, Texas 77843

L. Pienkowski
Heavy Ion Laboratory, Warsaw University, 02-093 Warsaw, Poland

R. G. Korteling
Department of Chemistry, Simon Fraser University, Burnaby, British Columbia, Canada V5A 1S6

H. Breuer
Department of Physics, University of Maryland, College Park, Maryland 20742

(Received 19 December 2000; revised manuscript received 1 June 2001; published 6 November 2001)

The event-by-event reconstruction procedure and related uncertainties involved in the derivation of excitation energy and source-size distributions are investigated for GeV hadron-induced reactions. The analysis is performed for the 5.0–14.6 GeV/c proton-, π^- and antiproton-induced reactions on ^{197}Au, measured with the Indiana silicon sphere charged-particle detector array at the Brookhaven AGS accelerator. The relative contributions of the three major components of the excitation-energy calorimetry: charged-particle kinetic-energy sums, neutrons, and Q values from reconstructed events, are found to be relatively constant for excitation energies above about 500 MeV. Effects on the results imposed by various assumptions necessary to account for experimental factors are examined and a corresponding deconvolution of the excitation-energy distribution is performed. The major uncertainties in the calorimetry are found to be (1) separation of nonequilibrium and thermal-like charged particles, and (2) the unmeasured neutron component. The self-consistency of the procedure is tested via comparisons with the SMM and SIMON codes for the disintegration of hot nuclei.

DOI: 10.1103/PhysRevC.64.064603 PACS number(s): 25.70.Pq, 21.65.+f, 25.40.−h, 25.80.Hp

I. INTRODUCTION

Studies of hot nuclei formed in the interaction of energetic projectiles with complex nuclei are important for providing insight into the thermodynamic properties that govern the nuclear equation of state [1,2]. Central to such investigations is the determination of the heat content of the excited heavy residue formed in these collisions. Only during the past decade have advances in the technology of detector arrays and the corresponding data-acquisition facilities permitted the large-acceptance measurement of thermal-like-particle spectra necessary to quantify the heat content.

One of the major goals of studies of hot nuclei is to search for the existence of a liquid-gas phase transition in finite nuclear systems. Several statistical calculations have predicted the expected features of this transition and have accounted for many experimental observables [3–6]. Comparisons of data and theory require the transformation of measured quantities into the thermodynamic variables necessary to describe the emitting source: heat content, temperature, source charge and mass, and density. The heat content, or excitation energy E^*, and source mass A_s and charge Z_s have been derived in several experiments using large detector arrays [7–12]. Various methods have been employed for measurement of nuclear temperatures: spectral slopes of the Maxwellian spectra, populations of excited states [13], and double-isotope ratios [14]. Source densities can be estimated from model simulations, [4,5,15], imaging techniques [16], and moving-source fits to the kinetic-energy spectra [17,18]. However, in all cases, complications arise due to the rapid time evolution of these hot nuclear systems and the necessity to establish at least quasiequilibrium in order for thermodynamic concepts to have relevance. Further considerations are the separation of thermal and collective features of the multifragmentation process and finite-size effects.

Ideally, the determination of excitation energies requires

*Present address: Laboratoire de Physique Corpusculaire de Caen, F-14050 Caen Cedex, France.
†Present address: Département de Physique, Université Laval, Quebec, Canada G1R 2J6.
‡Present address: Los Alamos National Laboratory, Los Alamos, NM 87545.
§Present address: Rush Presbyterian, St. Luke Medical Center, Chicago, IL 60612.
‖Present address: Barnes Hospital, Washington University, St. Louis, MO 63130.
¶Present address: Microcal Software, Inc., One Roundhouse Plaza, Northampton, MA 01060.
**Present address: Mallinckrodt Institute of Radiology, Washington University School of Medicine, St. Louis, MO 63110.

measurement of the emission angle, charge, mass, and kinetic energy of all emitted particles on an event-by-event basis. In practice, none of the existing detector arrays achieve this goal and, therefore, assumptions must be made in the event reconstruction to account for the unmeasured quantities; e.g., corrections for geometric factors, undetected neutral particles and/or kinetic-energy acceptance of the detector array. Hence, it is essential to investigate the uncertainties associated with determination of the excitation energy, mass, and charge for these thermal-like sources.

In this paper we focus on the event-by-event reconstruction of excitation energy and source charge for the following hadron-induced reactions on a ^{197}Au target: 6.2–14.6 GeV/c protons, 5.0–9.2 GeV/c π^-, and 8.0 GeV/c antiprotons. We examine the sensitivity of the deduced source properties to various assumptions contained in the event reconstruction procedure. We first present the experimental details, followed by a description of the reconstruction protocol and analysis of the various factors that influence the final results, the most important of which involve corrections for neutron kinetic energies and separation of thermal and nonthermal components of the spectra. Finally, we conclude with a summary of the values adopted for subsequent physics interpretations of these data, discussed in the following paper.

II. EXPERIMENTAL DETAILS

This paper presents results obtained with the Indiana silicon sphere (ISiS) 4π charged-particle detector array [19] in two experiments (E900 and E900a) at the Brookhaven National Laboratory AGS accelerator.

In E900 untagged secondary positive beams of momentum 6.0, 10.0, 12.8, and 14.6 GeV/c and negative beams at 5.0, 8.2, and 9.2 GeV/c bombarded a ^{197}Au target. In E900a a tagged beam of 8.0 GeV/c π^- and antiprotons was incident on a ^{197}Au target. The event-reconstruction and calorimetry procedures are described as applied to 1.2×10^7 events from the E900/E900a data that met the minimum bias trigger conditions (as described below). For consistency we have selected one system for presentation, 8.0 GeV/c π^- + ^{197}Au, which is representative of all the other reactions.

For both E900 and E900a average beam intensities were approximately $2-4\times10^6$ particles/spill, with a cycle time of 4.3 s and flat top of 2.2 s. The ^{197}Au target foils used in both experiments were prepared from 10^{-5} purity metal by vacuum evaporation onto a glass slide, using a KCl substrate that was subsequently removed by repeated washing. Two targets, 1×1 cm^2 and 2×2 cm^2 in area and 1.8–2.0 mg/cm^2 in thickness, were used to define the beam-target geometry. In order to provide a self-supporting target with minimum extraneous material exposed to the beam halo, each target was supported by two 50 μm gold-plated tungsten wires attached to a 5.0 cm$\times$5.0 cm target frame. A blank target was also inserted into the beam periodically to monitor the level of possible nontarget contributions to the spectra.

The ISiS detector array consists of 162 triple-detector telescopes arranged in a spherical geometry. The telescopes span the polar-angle range from 14°–86.5° in five segments in the forward hemisphere and 93.5°–166° in four backward-hemisphere segments. The azimuthal coverage consists of 18 telescopes in an annular ring, each subtending ~20° in azimuthal angle. The most forward ring is divided into two polar-angle segments. Total solid-angle coverage was 72% for the active telescopes in these experiments.

The detector telescopes consisted of a gas-ionization chamber operated at 16–18 Torr of C_3F_8 gas, a 500 μm passivated silicon detector, and a 28 mm CsI scintillator with photodiode readout. Additional details of the detector design are given in [19]. The energy acceptance for intermediate-mass fragment (IMF: $3\leqslant Z\leqslant16$) charge identification was $1.0\leqslant E/A\leqslant90$ MeV. Isotope identification was possible for light-charged particles (LCPs) with kinetic energy per nucleon $E/A\geqslant8$ MeV (LCP: H and He isotopes). In addition, all ejectiles that deposited energies $\geqslant$16 MeV in the CsI detector (but with the fast silicon signal too low to trigger the corresponding discriminator) were recorded for each accepted event, along with the recorded silicon slow energy signal. This provided information on the multiplicity of fast cascade ejectiles with energies up to ~350 MeV. This definition corresponds approximately to that of ''gray particles'' (forward-peaked LCPs originally identified in emulsion studies on the basis of track densities, intermediate between the evaporative and minimum ionizing particles E_{gray} ~100–1000 MeV).

In experiment E900 the composition of the positive beam, as indicated by AGS secondary production tables, ranged from about 90% proton/10% π^+ at the highest momentum to 60% proton/40% π^+ at the lowest momentum. The negative beam composition was predicted to be >95% π^-, a few percent K^- and about 1% $\bar{p}$ for the momenta studied here. For the purposes of this investigation, we identify the positive beam with protons and the negative beam with π^-. The rationale for this assumption is based on the insensitivity of the charged-particle multiplicity distributions to beam momentum or hadron type in these experiments [20]. The ISiS trigger was complemented by a 15 cm$\times$15 cm upstream total beam counter (TB), an annular ring veto scintillator (RV), a 28 mm$\times$28 mm beam-definition counter (BC), and a segmented inner/outer scintillator array (UV) upstream from the target for halo, veto, and beam alignment. The acceptance trigger logic was $\mathrm{TB}\cdot\overline{\mathrm{RV}}\cdot\mathrm{BC}\cdot\overline{\mathrm{UV}}\cdot$ ISiS.

The second experiment (E900a) was performed with a tagged secondary beam of 8.0 GeV/c negative particles (π^-,K^-,$\bar{p}$). Beam particles were tagged with a time-of-flight (TOF)/Cerenkov-counter identification system. The time-of-flight system employed a 12-mm-thick Bicron 418 plastic scintillator as a start detector and a 5-mm-thick Bicron 418 scintillator 64 m downstream as a stop element. Timing resolution (σ) was ≈200 ps and provided clean separation of $\bar{p}$ and π^- projectiles (8:1 peak-to-valley ratio), as shown in Fig. 1. This permitted simultaneous measurement of the $\bar{p}$ and π^- reactions under identical conditions. Beam composition was ≈98% π^-, 1% K^-, and 1% $\bar{p}$ at the target. For antiprotons a 7 m CO_2 gas Cerenkov counter operated at atmospheric pressure was used to identify and veto in software negative pions that overlapped with the $\bar{p}$ distribution in the time-of-flight spectrum, as shown in Fig. 1. A

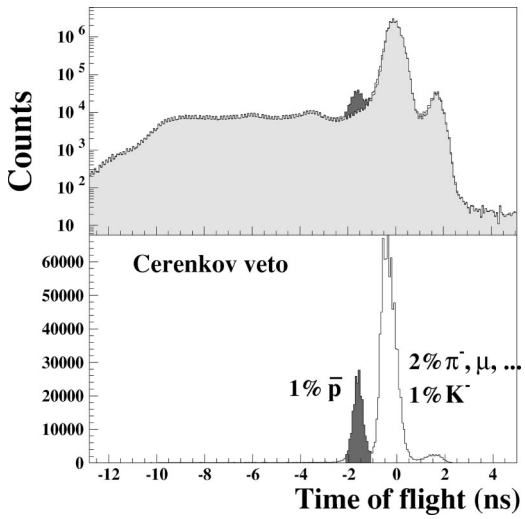

FIG. 1. Spectrum of tagged 8.0 GeV/c negative beam particles, showing total time-of-flight spectrum (top) and spectrum gated on Čerenkov counts (bottom).

segmented halo-veto scintillator array, described in Ref. [20], operated in anticoincidence with the TOF-$\check{C}$-ISiS coincidence signals. The experimental layout is shown in Fig. 2. Also, unidentified (''gray particles'') with energies from 92 to 350 MeV were measured. The minimum-bias ISiS hardware trigger required fast signals in three or more silicon detectors, but did not include ''gray particles.''

III. CALORIMETRY METHOD

Excitation-energy distributions in GeV hadron-induced reactions have been measured by two groups, the E900 Collaboration and the PS208 Collaboration at CERN. At LEAR, the PS208 collaboration have determined excitation energy distributions in 1.2 GeV antiproton-induced reactions [12]. They employed a method that measured LCPs and light IMFs along with the neutron multiplicity for each event. The PS208 excitation-energy reconstruction proceeded via two steps. First, a relation between the light particle multiplicity ($M_{\rm LP}$) and the excitation energy (E^*) was established from the statistical model code GEMINI [21]. Then the light particle multiplicity is measured with the Berlin neutron ball [22] and the Berlin silicon ball [23]. Finally, the excitation energy is derived event by event from the relation between the measured light-particle multiplicities and those predicted by the codes.

The ISiS collaboration has chosen another method that relies on a balance energy (calorimetric procedure) made event by event [7–10,24,25]. This method exploits one of the major advantages afforded by hadron projectiles in the study of multifragmentation; i.e., the ability to separate the nonequilibrium and equilibriumlike components of the reaction. This separation, albeit imperfect, is facilitated by the different shapes of the high- and low-energy components of the kinetic-energy spectra of the emitted particles [17,18]. As seen in Fig. 3, for LCPs two components are clearly distinguishable in the inclusive spectra, which are schematically attributed to equilibriumlike and nonequilibrium mechanisms.

The nonequilibrated component originates in the cascade of pions and nucleons induced by the incident projectile in the target nucleus and is composed mainly of neutrons, H, He, and Li ions. In this paper these energetic ions are subtracted from the target charge in order to obtain the charge of the thermal-like sources, but are not used otherwise.

In E900 and E900a the excitation energy was derived from the thermal-like decay products via the equation

$$E^* = \sum_i^{M_{\rm cp}} K_i^{\rm cp} + M_n \langle K_n \rangle + Q + E\gamma. \qquad (1)$$

Here the $K_i^{\rm cp}$ are the measured kinetic energies of thermal-like charged particles in an event of multiplicity $M_{\rm cp}$, transformed into the source frame. To account for the unmeasured neutrons, we use an average multiplicity M_n as a function of $M_{\rm cp}$ and a corresponding average neutron kinetic energy K_n, as described in Sec. IV. Q is the mass-energy difference between the final products and the initial thermal-like source. Energy released in gamma emission is assumed to be $E\gamma = M_{(Z\geqslant 3)} \times 1$ MeV. Corrections are included to account for the ISiS geometry.

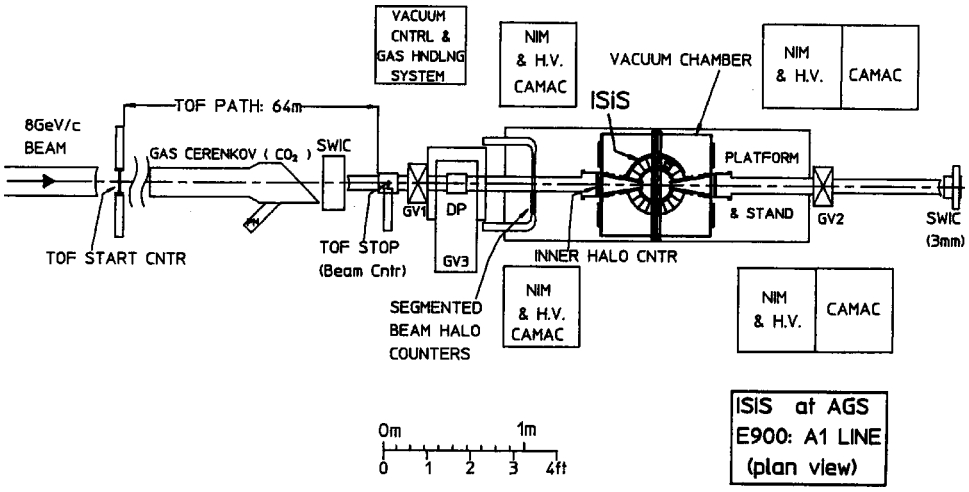

FIG. 2. Schematic layout of apparatus used in studies of the 8.0 GeV/c $\pi^- + {}^{197}$Au reaction.

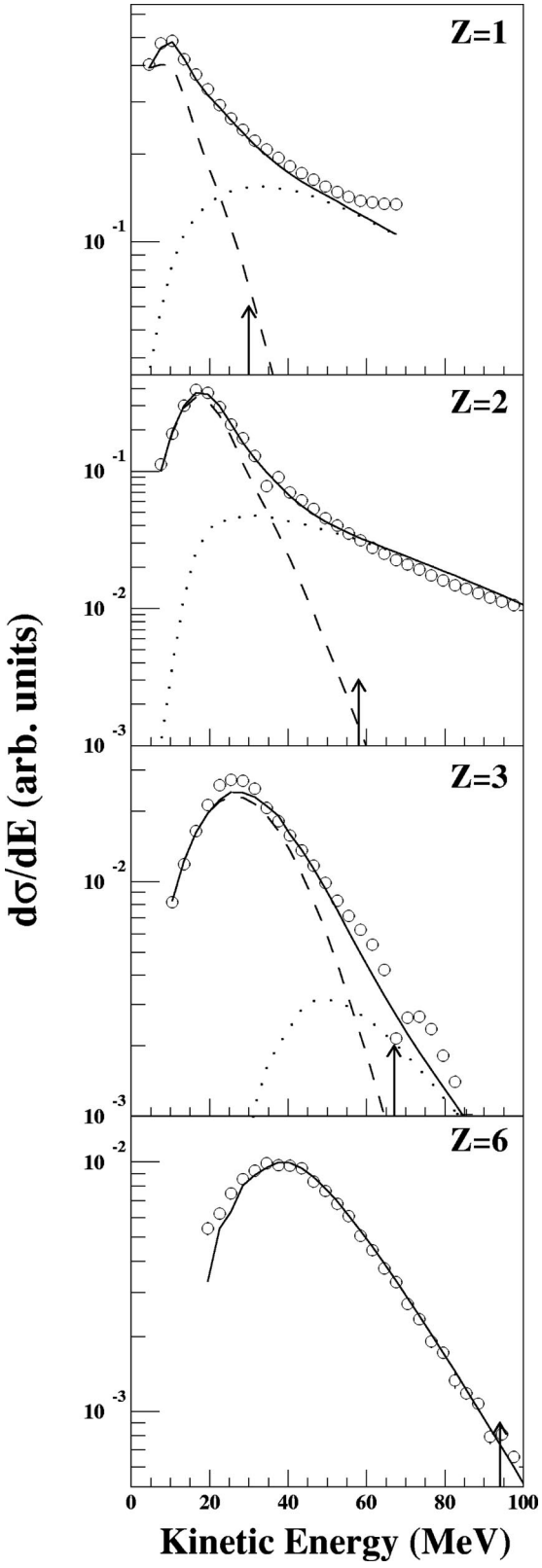

FIG. 3. Angle-integrated kinetic-energy spectra in the laboratory for $Z=1$, 2, 3, and 6 as indicated in each panel. Open points correspond to data. Dashed (dotted) lines represent the thermal-like (nonequilibrated) component of the moving-source fit. The solid line is the sum of the two fits. Upper cutoff energies [27] are shown by vertical arrows.

The charge and mass of the excited source are determined on an event-by-event basis by subtracting the nonequilibrated particles from the target charge and mass

$$Z_s = Z_{\mathrm{tgt}} - \sum_i^{M_{\mathrm{neq}}} Z_i^{\mathrm{neq}}, \tag{2}$$

and

$$A_s = A_{\mathrm{tgt}} - \sum_i^{M_{\mathrm{neq}}} Z_i^{\mathrm{neq}} + \langle M_n^{\mathrm{neq}} \rangle, \tag{3}$$

where Z_s, A_s are the charge and mass of the emitting source, $Z_{\mathrm{tgt}}, A_{\mathrm{tgt}}$ are those of the initial target, Z_i^{neq} is the charge of shower/nonequilibrated (neq) particles i, and $\langle M_n^{\mathrm{neq}} \rangle$ is the average multiplicity of nonequilibrium neutrons. Efficiency corrections, taking into account the forward focusing of nonequilibrium emission, are included to account for ISiS geometry. More details about the definition of the nonequilibrated component are given in Secs. IV and V.

For all probability distributions shown in this work the total number of events is normalized to unity. It is estimated that the total cross section for measured events in E900 is $\sigma \approx 1300 \pm 200$ mb relative to a geometric cross section of $\sigma_{geo} = 2100$ mb, as discussed in the following paper [26].

IV. CHARACTERIZATION OF THE THERMAL-LIKE SOURCE

Since the shower/nonequilibrium particles leave the target nucleus prior to thermalization, they must be removed from the kinetic energy and charge(mass) sums in performing the calorimetry. In Fig. 3 the inclusive angle-integrated kinetic-energy spectra are plotted for H, He, Li, and C nuclei. Because the kinematic tranformations are small ($v_{\parallel}/c \lesssim 0.01c$), the laboratory spectra do not show a pronounced angle dependence. The high-energy tails above the Coulomblike peaks show two exponential slope components for the LCPs; one corresponding to the tail of a thermal-like spectrum and one to a higher-energy component. We associate the latter with nonequilibrium emission. The nonequilibrium component is less apparent for Li and nearly absent for C. For fragments with $Z \geqslant 6$ only a single component is discernible in the spectra at the 10^{-3} probability level. Here we define all distributions in terms of a unit probability $\Sigma_i P(n_i) = 1$ for each set of events n_i relative to the total number of events N.

In order to perform the separation between the thermal-like particles and the nonequilibrium ones, two-component moving-source fits have been performed as a function of angle [17,18,27]. The parametrization, given by Eq. (20) of Ref. [28], has been used for the thermal-like source. This model assumes surface emission from a nucleus at normal density with charge Z_s, velocity v, temperature T, fractional Coulomb barrier K_c, and spectral shape parameter p. The nonequilibrated source is assumed to be described by a standard Maxwellian function. Since the main purpose of the two-component fits is to define a systematic method to isolate thermal-like emission, we will not discuss the extracted parameters.

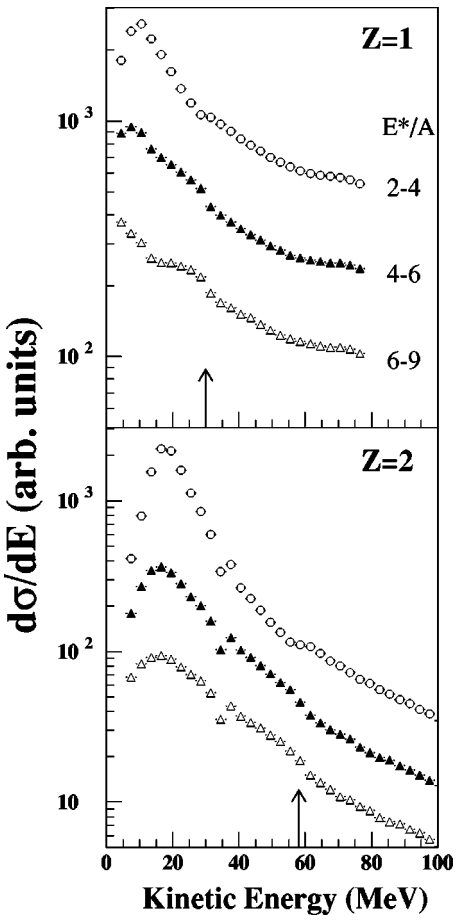

FIG. 4. Angle-integrated kinetic-energy spectra in the laboratory for $Z=1$ and $Z=2$ as indicated in each panel, and for three bins in E^*/A calculated with the cutoff assumption of Eqs. (4) and (5) [27]. The symbols correspond to $E^*/A=2-4$ (open circles), $E^*/A=4-6$ (filled triangles), and $E^*/A=6-9$ MeV (open triangles) bins.

Based on this procedure, thermal-like particles were defined by a sharp cutoff approximation for the 1.8–4.8 GeV ^{3}He+ ^{197} Au reactions [27]

$$K(Z=1)\leqslant 30 \text{ MeV}, \tag{4}$$

$$K(Z\geqslant 2)\leqslant (9Z+40) \text{ MeV}. \tag{5}$$

This schematic definition is consistent with the present spectra and is adopted here. These sharp cutoff energies are shown in Figs. 3 and 4, by vertical arrows. Figure 4 shows the angle-integrated spectra for $Z=1$ and 2 ions as a function of E^*/A. With increasing excitation energy the break in the slope becomes less distinct and can be described by a single source at the highest excitation energies. Thus, the separation of the two components near the cutoff energies is blurred because of the time evolution of the reaction; i.e., experimentally one cannot distinquish between a late nonequilibrium particle and a short statistical emission time. The sharp cutoff assumption of Eqs. (4) and (5) leads to an underestimate of E^* at high excitation energies if a thermal-like source produces these particles.

As an alternative approach, we define a second assumption in order to give a lower estimate of the excitation energy as well as source charge. Using the moving-source fits, the probability that a particle is either a thermal or nonequilibrium particle is obtained from the respective relative yields of the two spectral components normalized to the total yield. At a given kinetic energy, a particle is thus defined by two probabilities related by the following equation:

$$P_{\text{ke}}(\text{th})+P_{\text{ke}}(\text{neq})=1. \tag{6}$$

Thermal probabilities $P_{\text{ke}}(\text{th})$ of each particle are used in the energy and mass balance sums of Eq. (1) in order to determine the excitation energy and source charge. The dashed and dotted lines in Fig. 3 represent, respectively, thermal and nonequilibrated fits from which probabilities have been extracted. Due to the assumption about the function (Maxwellian) used to fit the preequilibrium emission and the large number (ten) of parameters of the fitting procedure, several fits with similar chi-squared values may be found. For proton spectra, we purposely used a lower estimate of the thermal-like component in order to minimize the excitation energy.

In Fig. 5 a check of the consistency of both methods is performed by looking at the angular distributions for thermal-like particles (shaded area) and for all particles (white area) in the laboratory frame. The anisotropic contribution of fast nonequilibrium particles is removed for $Z=1$ and $Z=2$ when the cutoff energy assumption is applied, as indicated by the shaded curves in the left panels of Fig. 5. The remaining forward focusing of the thermal component is due to the longitudinal velocity component of the emitting source [29]. This has been checked by using a simulation of an isotropically-decaying source (thick plain line in Fig. 5) moving with longitudinal source velocity $v_{\parallel}$ extracted from the thermal source fits. The calculation is passed through the ISiS filter and is normalized to the data points of the $\Theta_{\text{lab}}=128^\circ-147^\circ$ ring of ISiS. Except for $Z=3-5$, the thermal-like particles are well described by isotropic emission from a source moving with velocity $v_{\parallel}\lesssim 0.01c$.

In the left middle panel of Fig. 6, the total excitation-energy distribution with the sharp cutoff assumption is seen to extend to higher E^* values than that which uses the moving-source fits. Arrows indicate the position of the lower limit of the last one percent ($\sim$13 mb) of all measured events for each distribution, i.e., $E^*=1150$ MeV for the sharp cutoff assumption and $E^*=975$ MeV for the moving source fit. The relative difference between the two estimates, goes up to 17% at $E^*(\text{cutoff})=1150$ MeV as shown in the left bottom panel of Fig. 6.

In contrast to the E^* results from the moving-source fits, analysis of the EOS data [30] has imposed a nonequilibrium sharp cutoff assumption of $E/A\leqslant 30$ MeV. This approach yields excitation energies about 20% higher than for the assumptions of Eqs. (4) and (5), as shown in Fig. 7. The origin of this difference is the inclusion of large contributions to the excitation energy sum of $A=2-4$ particles in EOS that fall well above the cutoffs established by the spectral shapes observed in ISiS.

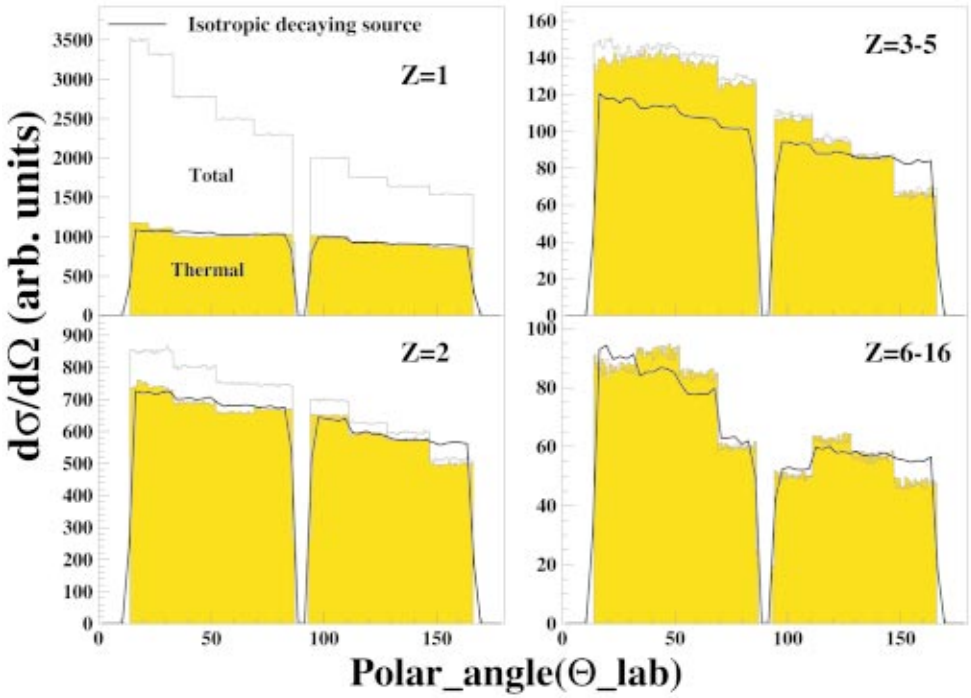

FIG. 5. (Color) Angular distributions in the laboratory for $Z=1$, $Z=2$, $Z=3-5$, and $Z=6-16$, as indicated in each panel. Yellow areas correspond to thermal-like components; white ones to global components. The thick plain line represents the angular distribution of an isotropically decaying moving source (see text for more details). For each panel the simulation is normalized to the data points of the eighth ring of ISiS ($\Theta_{\rm lab}=128°-147°$). The lack of counts at forward ($\Theta_{\rm lab}=0°-14°$) and backward ($\Theta_{\rm lab}=166°-180°$) angles correspond to beam apertures and at middle angles ($\Theta_{\rm lab}=86.4°-93.6°$) to the target ladder.

In the right middle panel of Fig. 6 the more relevant quantity E^*/A shows smaller deviations between the sharp-cutoff and moving-source assumptions. Maximum deviations of $\sim$12% occur near $E^*/A\sim 6$ MeV, as shown in the bottom right panel of Fig. 6. Since a high cutoff energy reduces the number of nonequilibrium particles, the corresponding source mass is also larger, thus cancelling out the increase in E^*. For example, at the level where all but the last one percent of the data are accounted for, the moving source assumption yields $E^*/A\approx 7.5$ MeV, which is about 8% lower than that obtained with Eq. (4) and Eq. (5). For the uniform $E/A\leqslant 30$ MeV cutoff assumption, a value of $E^*/A \simeq 9$ MeV is obtained, which is about 12% higher.

The upper panels of Fig. 6 show the decrease in the average source charge, normalized to the target charge and determined with both the sharp cutoff [27] and moving-source assumptions, as a function of excitation energy. This decrease arises from the fact that as the excitation energy increases, nonequilibrated emission increases as well, which leads to lower source mass as the excitation energy increases. At the lower limit of the last 1% of each distribution, the source size is about 80% of the initial target size using the thermal-energy acceptance of Eqs. (4) and (5) and 70% with the moving-source fits. The discrepancy between the two estimated source charges (mass) increases up to 12% at $E^* = 1150$ MeV ($E^*/A=8$ MeV).

In our adopted excitation-energy distributions, we use the sharp cutoff assumption of Ref. [27] as an intermediate approach between the two-source fits and the EOS approach.

V. CORRECTIONS FOR NEUTRON EMISSION

For all 4π charged-particle detector arrays, the second major uncertainty regarding the excitation-energy procedure is the estimation of (1) the neutron multiplicities for thermal-like and nonequilibrium/sources and (2) the kinetic energy contribution for neutrons from the thermal-like source. In this analysis the nonequilibrium neutron multiplicity is taken to be $M_n^{\rm neq}=1.93M_p^{\rm neq}$, where $M_p^{\rm neq}$ is the nonequilibrium proton multiplicity. This assumption is consistent with Boltzmann-Uehling-Uhlenback, calculations [31], recent experimental data [32] and is intermediate between previous estimates based on the N/Z of the target and the experimental systematics of [33].

In order to estimate the thermal-like neutron component, we used the neutron-charged particle correlations reported for 1.2 GeV $\bar{p}+{}^{197}$Au reactions by Goldenbaum *et al.* [12]. At low charged-particle multiplicity the neutron multiplicity rises sharply and then increases much more gradually beyond $\langle M_n\rangle\approx 15$, as shown in Fig. 8. The correlation is reasonably well described by two model simulations, SMM [4] and SIMON evaporation [15] for charged particle multiplicity $M_c>4$. The inputs to both models are the source charge, mass and excitation energy, extracted from ISiS data. The same qualitative behavior has been observed in heavy-ion reactions [34], indicating that at low excitation energies neutron emission is the primary emission mode. As the excitation energy increases and source N/Z decreases, charged-particle emission grows in probability relative to neutron emission.

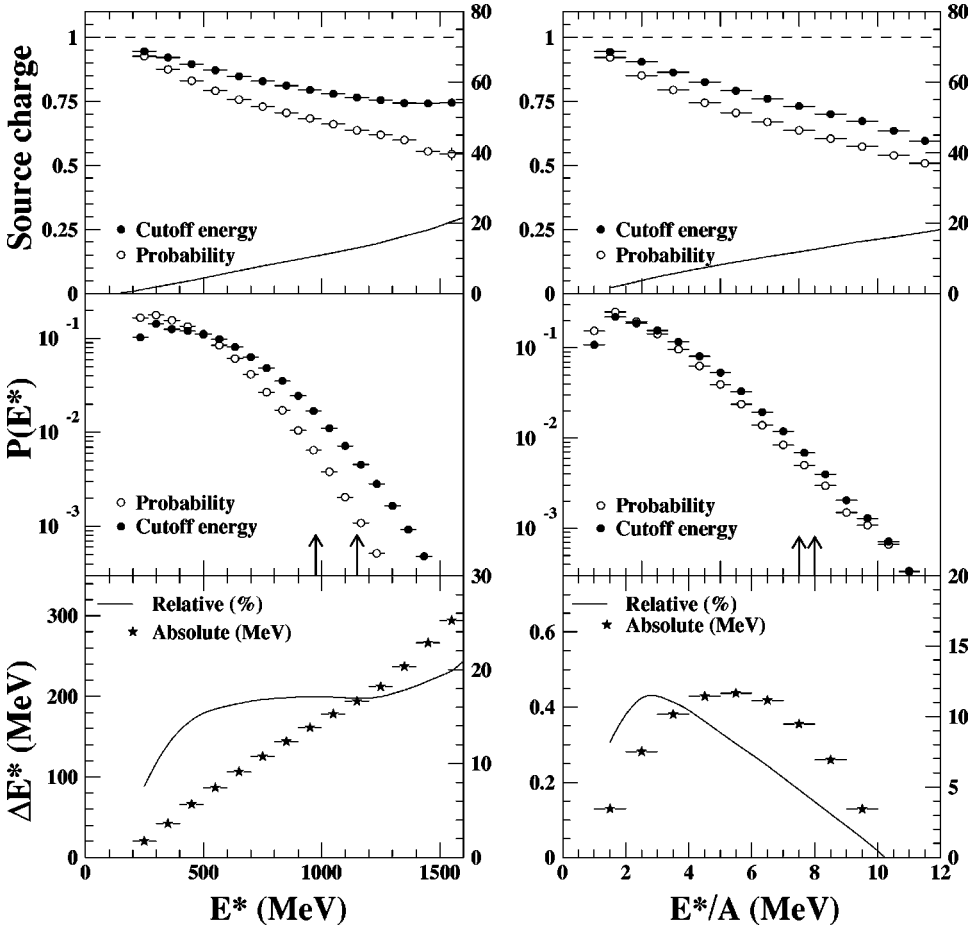

FIG. 6. The upper (middle) panels represent the mean source charge (the excitation-energy distributions) determined with two different assumptions regarding nonequilibrated emission, the sharp cutoff of Eqs. (4) and (5) (closed circles) and the moving source fits (open circles). The solid line is the relative difference between the two estimated mean charges (measured by the right scales). The dashed line refers only to the left-handed scale. Arrows in the middle panels represent values above which the last 1% of each excitation-energy distribution occurs. The lower panels correspond to the absolute (black stars) and relative (solid lines) differences between excitation energies determined with the two assumptions regarding the nonequilibrated emission. The right scale on each figure gives the relative differences, and the left scale the absolute differences. Variables are displayed as a function of E^* in the left panels and E^*/A in the right panels.

One can also use a mass balance procedure in order to estimate the multiplicity of free neutrons [10,24,30,34]. The number of free neutrons is then determined as follows:

$$M_n = (A_s - Z_s) - [(A_{\text{emitted}} - Z_{\text{emitted}}) + (A_{\text{missing}} - Z_{\text{missing}})], \tag{7}$$

where A_s, Z_s are derived from Eqs. (2) and (3); $(A_{\text{emitted}}, Z_{\text{emitted}})$ are the total mass and charge of all emitted thermal products, and Z_{missing} is the total undetected charge. A_{missing} is then determined from Z_{missing} with respect to the valley of stability or by assuming the conservation of the initial N/Z ratio. The mass balance assumption (open squares in Fig. 8) does not reproduce the experimental correlation. Indeed, all considered masses (emitted fragments and missing mass) have been estimated using the stability valley and,

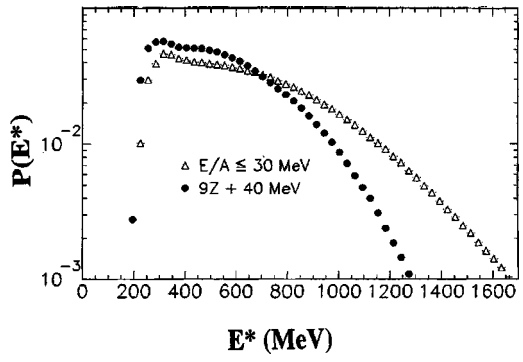

FIG. 7. Excitation-energy distributions for sharp cutoff assumptions of Eqs. (4) and (5) compared with a cutoff value of $E_k/A_{\text{IMF}} < 30$ MeV.

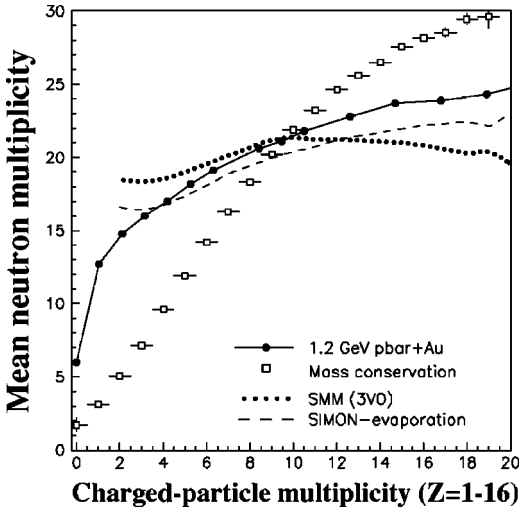

FIG. 8. Relation between the mean neutron multiplicity and the charged-particle multiplicity. Solid line corresponds to data points reported for LEAR data by Ref. [12]; solid line is SMM calculation, and SIMON evaporation is given by the dashed line. The open squares give the mean multiplicities estimated with the mass conservation assumption [10,21,25,29].

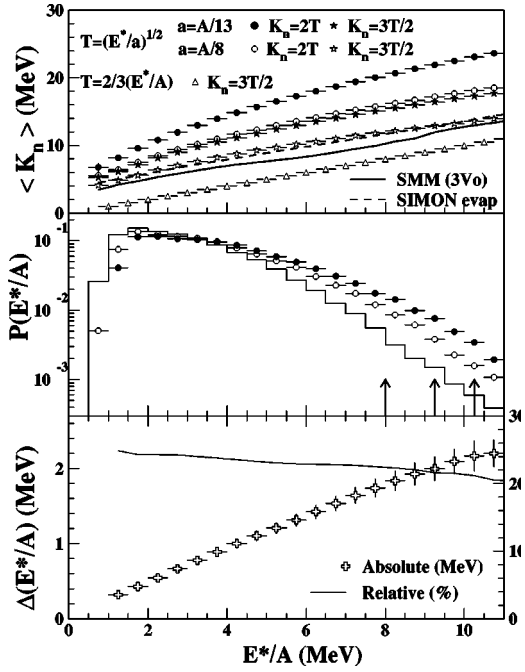

FIG. 9. Upper panel: estimates of neutron mean kinetic energy as a function of excitation energy per nucleon, as indicated in panel. Middle panel: $P(E^*/A)$ distributions for three different assumptions regarding neutron kinetic energy; the solid line corresponds to the SMM assumption at one-third normal density, the open circles to a Fermi-gas assumption with $a=A/8$ MeV^{-1}, and the filled circles to $a=A/13$ MeV^{-1}. Distributions are normalized to total number of events. Lower panel: discrepancy between excitation energy per nucleon determined with the SMM assumption and with a Fermi-gas assumption with $a=A/13$ MeV^{-1}. Note: the right scale is for relative discrepancies, and the left scale for absolute errors.

therefore, do not account for the important emission of neutrons at low charged-particle multiplicity and the saturation at high multiplicity. The same effect is observed when one uses the initial N/Z ratio to extract the missing mass from the missing charge.

As far as the neutron kinetic energy is concerned, none of the detector arrays measure this quantity over 4π in coincidence with charged particles. In order to estimate this important effect, several assumptions can be used, as shown in the upper panel of Fig. 9. For all of them the mean neutron kinetic energy is taken from the correlation between $\langle K_n \rangle$ and E^*/A and then Eq. (1) is iterated in order to obtain self-consistency.

In the top panel of Fig. 9, one can already notice the large discrepancy in the average neutron kinetic energy as a function of E^*/A between the Fermi-gas assumption (open and filled circles) and a Maxwell-gas assumption (open triangles). Formally, the former can only be used at low E^*/A and the latter at high E^*/A. Neither takes into account the intermediate E^*/A range where a first-order phase transition may take place. However, in order to use the $K_n=2T_s$ (surface emission) or $K_n=3T_s/2$ (volume emission) relations [35], the temperature of the source must be determined. For the Fermi-gas assumption it is extracted via the relation $T_s=\sqrt{E^*/a}$ [8–10,25], where the level-density parameter a ranges from $a=A/13$ MeV^{-1} to $A/8$ MeV^{-1} [36]. For the Maxwell-gas assumption, $T_s=2/3(E^*/A)$. In both cases E^*/A is the total (initial) excitation per nucleon and T_s is the initial temperature. Consequently, the cooling of the source along the decay chain is neglected, leading to an overestimation of the average neutron kinetic-energy. In Fig. 9 the neutron kinetic energy overestimation is clearly seen when one uses the relation $K_n=2T_s$ in conjunction with Eq. (1).

In order to compare the predictions of model calculations with the various T_s assumptions relative to the mean neutron kinetic energy, two calculations, SMM [4,37] and SIMON-evaporation [15], have been performed (top panel of Fig. 9). Both models take into account the time-dependent cooling effect. The neutron emission in both cases is mainly described by a sequential surface emission. Indeed, in SMM at least 90% of all emitted neutrons come from secondary decay of heavy decaying fragments [37]. In SIMON evaporation the level-density parameter is set to $a=A/10$ MeV^{-1}, in SMM to $a=A/9$ MeV^{-1}.

In the middle panel of Fig. 9, the resulting probability distributions for the total excitation energy appear in the E^*/A distribution for the Fermi-gas assumption with $K_n=2T_s$ and the SMM model. Locations of the lower limit of the last 1% of each distribution are $E^*/A=10.25$ and $E^*/A=9.25$ for the two Fermi-gas assumption, with, respectively, $a=A/13$ MeV^{-1} and $a=A/8$ MeV^{-1}, and $E^*/A=8$ MeV when $\langle K_n \rangle$ is taken from SMM. The relative difference is about 20% over the whole range of excitation energy, as indicated in the lower panel of Fig. 9.

Finally, several groups have used the relation $K_n=C_{\rm eff}\,T_s$ with the Fermi-gas assumption $T_s=\sqrt{(E^*/a)}$ and $C_{\rm eff}=3/2$. In that case, the coefficient $C_{\rm eff}$ is lower than 2 in order to take into account the cooling of the source and has nothing to do with the Maxwell-gas assumption. Using this procedure, a good agreement is found with SIMON-evaporation calculation when the level-density parameter is set to $a=A/8$ MeV^{-1}, as indicated by the open stars in the top panel of Fig. 9. For $a=A/13$ MeV^{-1}, the mean neutron kinetic energy is overestimated (black stars). Good agreement is also found when one uses $K_n=T_s$ ($C_{\rm eff}=1$) with a level-density parameter increasing from $a=A/10$ MeV^{-1} at $E^*/A=1A$ MeV to $a=A/13$ MeV^{-1} at $E^*/A=5A$ MeV [38].

In our adopted procedure, we have used the SMM prediction as a conservative estimate of the excitation-energy contribution from neutron kinetic energies.

VI. ADDITIONAL FACTORS

Besides the two important factors indicated above, which can change the E^* values by 10–30 %, some second-order corrections have also been investigated.

(1) Source velocity—This factor was accounted for by using moving-source-fit velocity parameters derived as a function of total detected multiplicity. The velocity is small ($v_\parallel \leqslant 0.01c$) and has a minor impact.

(2) Source angle—For simplicity we have assumed in our reconstruction procedure that the source is moving along the beam axis, although intranuclear cascade calculations indicate a significant transverse velocity component [29]. As

long as the linear component of the source velocity is not much bigger than $0.02c$, the source angle does not have any significant effect.

(3) Geometrical efficiency corrections do not fold in particles with energies below the detector thresholds, especially heavy IMFs (because of small source velocity). This could produce a slight underestimation of E^* (Sec. VII).

(4) Final residue Z,A—The assumption that all missing charge and mass is contained in one residue works well at low E^*. However, as E^*/A increases beyond ~ 5 MeV, there may be two or more low-energy fragments. In that case, there is a tradeoff between the calculated Q value of one big residue, which minimizes E^*, compared to the Q value of many smaller particles and some missing kinetic energies ($\langle K_{cp}\rangle/A$ MeV per missing particle), which would increase E^*.

VII. MODEL COMPARISONS

In order to check the consistency of the calorimetry method used for these hadron-induced reactions measured with ISiS, the SMM and SIMON-evaporation calculations have been used as test cases. Both model simulations use identical input information, based on the experimental distributions of source charge, mass, velocity and excitation energy reconstructed from data [38,39]. Then the simulations are filtered to take account of the geometry of ISiS, the particle kinetic-energy thresholds and the energy lost in the target.

In Fig. 10 correlations between the initial and reconstructed excitation energies of the simulations are shown. For this purpose simulation particles above the thermal cutoffs of Figs. 4 and 5 have not been eliminated from the reconstructions. For each simulation the neutron mean kinetic energy is extracted from the respective model correlation displayed in the top panel of Fig. 9. The average reconstructed excitation energy, open circles in Fig. 9, is systematically underestimated with both simulations. Part of this underestimation is due to undetected charged products emitted below threshold. Most of the undetected charge corresponds to the charge of the largest fragment. Better agreement is found when one adds the energy lost below thresholds, which is a known quantity in simulations, to the standard reconstruction of excitation energy. Inclusion of this effect is indicated by the filled triangles in Fig. 9. The underestimation is about 5% of the excitation energy and goes up to 50 MeV at $E^* = 1100$ MeV for both model calculations and is independent of other assumptions, which can shift the excitation energy scale by 10–20 %. The remaining difference is due to the estimate of the neutron multiplicity, which differs between the models and the data from [12].

From both simulations it is also possible to extract the standard deviation of calculated excitation energies at a given initial excitation energy. The dispersion around the average value is mainly due to two effects: detector geometry and neutron assumptions (multiplicity and kinetic energy). Part of the dispersion from the preequilibrium emission is also taken into account in model calculations since the source charge and mass distributions, Eqs. (2) and (3), are used as inputs to the codes. Note that for each calculation the mean neutron kinetic energy is taken from the corresponding model. For both model calculations, the standard deviation is about $20\% \pm 5\%$. The detector geometry, 72% of 4π for ISiS, contributes about 8–10 % of the total standard deviation. The remaining part, 10–12 %, results from the neutron-reconstruction assumptions.

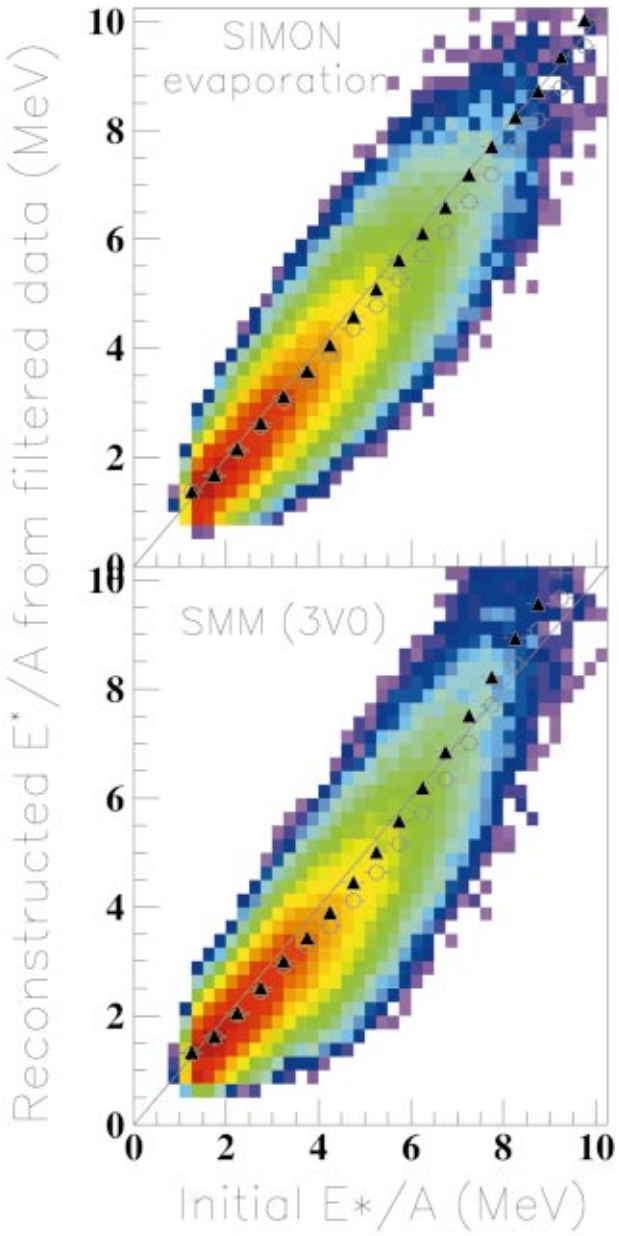

FIG. 10. (Color) Reconstructed E^*/A calculated as a function of initial E^*/A for SIMON evaporation (upper panel) and SMM (lower panel) models. The simulations are filtered with the experimental acceptance of ISiS.

VIII. RELATIVE CONTRIBUTIONS TO THE EXCITATION ENERGY

The relative share of the total excitation energy contributed by each of the major components in the reconstruction is shown in Fig. 11 as a function of E^*/A. These values

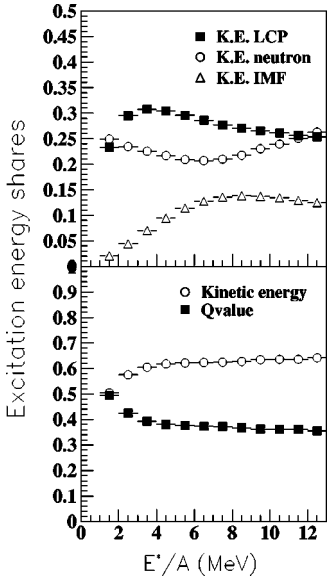

FIG. 11. Relative share of excitation energy for various components of the reconstruction procedure [Eq. (1)] as a function of $E^*/A_{\rm src}$. Top frame: light-charged particle kinetic energy (solid squares), neutron kinetic energy (open circles), and IMF kinetic energy (open triangles). Bottom frame: total particle kinetic energy (open circles) and Q values (solid squares)

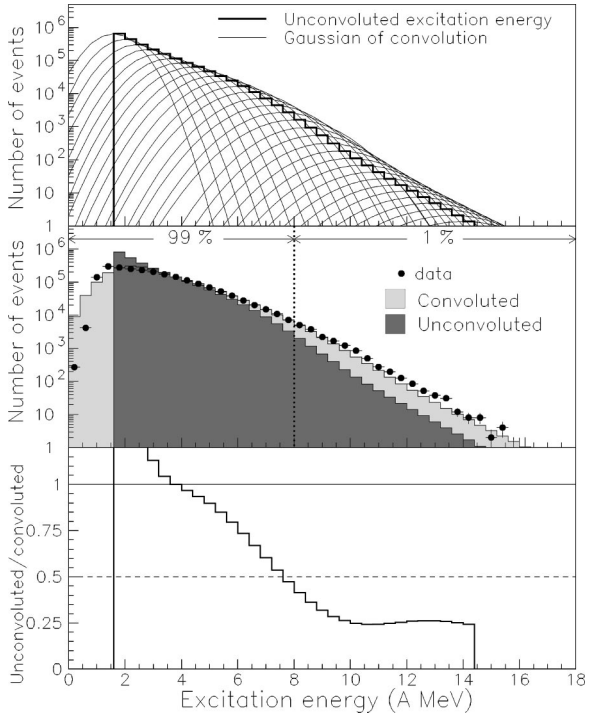

FIG. 12. Top panel: unconvoluted excitation-energy distribution and individual Gaussians of convolution, as indicated in the figure. Middle panel: convoluted (light gray curve), unconvoluted (dark gray), and experimental (filled circles) excitation-energy distributions. Distributions are normalized to the experimental values at $E^*/A=4$ MeV. The dotted line denotes $E^*/A_{\rm src}$ probabilities that account for the last 1% of the events. Bottom panel: ratio of the unconvoluted-to-convoluted distribution as a function of excitation energy per nucleon.

represent our final adopted protocol for reconstruction, the principal elements of which are (1) the total measured charged-particle kinetic energies; (2) the thermal-cutoff-energy definition of Eqs. (4) and (5); (3) the neutron-charged particle correlations of Ref. [12], and (4) the average neutron kinetic energies of the SMM model [37]. The top frames of Fig. 11 show that for $E^*/A \gtrsim 3$ MeV, light-charged particles and neutrons account for over half of the excitation energy, contributing nearly constant shares: 30% for LCPs and 20–25 % for neutrons. Over the same excitation-energy range, the IMF share increases from about 5 to 15 %; i.e., the IMFs make only a minor contribution to the total E^*.

When the relative contributions of the total-particle kinetic-energy sum and Q value are examined (bottom frame of Fig. 11), similar systematics are observed as a function of E^*/A. About 60–65 % is due to the kinetic-energy sum and 35–40 % to the Q values. Whereas the IMF kinetic-energy contribution is small, these fragments do play an important role in defining the fragment charge distribution within an event, necessary for the Q-value calculation. In summary, Fig. 11 indicates that for $E^*/A \gtrsim 5$ MeV, where the onset of multifragmentation is expected to occur, the ratios of the major contributions remain relatively constant, suggesting the reconstruction procedure is not being dominated by correlations other than the conservation of energy.

The maximum excitation energy that GeV/c hadrons can deposit in target nuclei is an important issue if one wants to study processes at the highest excitation energies. In order to determine this maximum value, one has to take into account two points. First of all, events with a total charge greater than the initial source charge are overcorrected due to detector efficiency and, therefore, lead to overestimated excitation energy. The effect of overcorrection is negligible below $E^*/A = 10$ MeV. Reconstructed events with $Z_{\rm th} > Z_s$ ($<0.01\%$) have been removed in the experimental excitation energy distribution shown in Fig. 12, where a detailed analysis of the tail of the distribution is performed.

The second source of overestimation is the dispersion involved in the excitation-energy calculation due to detector inefficiency and neutron assumptions. For the bulk of the excitation-energy distribution the overestimated E^* coming from lower true E^* and underestimated E^* coming from higher true E^* cancel each other. The estimate of excitation energy is, therefore, correct on average. On the other hand, in the tail of the distribution there are fewer events at high excitation energy than at low excitation energy. The average effect doesn't hold anymore and one observes a systematic overestimate of excitation energy.

In order to estimate the magnitude of this overestimate, one can convolute a given true excitation energy distribution assuming Gaussian-like fluctuations. In the top panel of Fig. 12, the average and the width of each Gaussian correspond, respectively, to the excitation energy bin value and the standard deviation extracted from the model comparisons in Fig. 10. The shape of the unconvoluted excitation-energy distribution, the thick plain line in Fig. 12, is chosen in order to give a convoluted distribution similar to the experimental

one. Here, the unconvoluted excitation distribution is given by the sum of a Gaussian and an exponential. The cutoff at low excitation energy corresponds to the detector trigger requirement. In the bottom panel of Fig. 12, distributions are normalized to each other at $E^*/A=4$ MeV, where the excitation energy reconstruction should be most reliable.

Overestimates due to the convolution effect are at about $1-2\,A$ MeV in the extreme tail of the distribution and $0.5-1\,A$ MeV at $E^*/A=8$ MeV. Above $E^*/A=7-8$ MeV, more than half of events have an overestimated excitation energy value as shown in the bottom panel of Fig. 12. On the other hand, our criteria for event reconstruction have attempted to minimize the resultant E^* values; for example, by using a model (SMM) for neutron kinetic energies primarily based on secondary decay from the fragments rather than the source, setting a low cutoff energy between thermal and nonequilibrium charged particles, and assuming all of the missing mass is contained in a single fragment rather than its constituent nucleons. A somewhat more relaxed set of acceptance criteria could easily shift the E^* scale upward by 10–20 %, while the difference between the convoluted and unconvoluted distributions would be about the same.

Under any circumstances, events with excitation energies well above the total binding energy of Au-like residues at normal density are observed in the unconvoluted distribution. Part of the extra excitation energy, i.e., above the binding energy of the nucleus, may be used in expansion of the nucleus, leading to larger reconstructed energy deposition.

IX. SUMMARY

In this study we have described the event-by-event reconstruction procedure employed in determining the excitation energy of thermal-like residues formed in GeV hadron-induced reactions on ^{197}Au. The prescription is based on the standard calorimetry assumptions of energy and mass balance. The ISiS array provides nearly complete coverage of all LCP and IMF spectra, with high statistics and 72% geometric coverage. The measured charged-particle kinetic-energy sum accounts for 35–40 % of the total excitation energy at moderate to high E^*. The charged-particle identification also permits a reliable calculation of the Q-value component (35–40 %). Thus, the measured spectra and Q values account for a total of 60–70 % of the total excitation energy. ISiS does not measure charged particles below $E/A<1$ MeV or neutrons (20–25 % of E^* above $\sim$500 MeV), which are accounted for on the basis of the measurements of Goldenbaum *et al.* [12]. We assume that all missing mass is contained in a single heavy fragment, again minimizing E^*.

The uncertainties generated by experimental factors and the assumptions involved in the reconstruction procedure are examined. Principal among these are the elimination of nonequilibrium particles from an event and the contribution of the unmeasured neutrons. The excellent kinetic-energy determination provided by ISiS permits a schematic separation of equilibriumlike and nonequilibrium events, based on the systematic slope changes in the spectral tails. We have adopted this protocol as a compromise between a two-component moving-source fitting approach, which yields lower E^* values, and a uniform thermal cutoff energy for particles with kinetic energy $E/A<30$ MeV, which results in higher E^*.

For the unmeasured neutrons our use of the neutron-charged particle multiplicities of [12] has a much greater effect on the fluctuations in our data than on the averages. The magnitude of E^* is influenced significantly by assumptions concerning the average neutron kinetic energy. Here we employ an assumption based on SMM simulations, which is significantly lower than values of $2T$, which have been employed in some calorimetry efforts. Other parameters are a small fraction of the uncertainties with respect to the nonequilibrium particles and neutrons; i.e., source velocity and emission angle, IMF thresholds, the single-fragment assumption for missing mass, and the nonequilibrium neutron multiplicity.

Overall, no component of E^* above $E^*\sim500$ MeV varies strongly with increasing excitation energy. The philosophy in selecting the final parameters for E^* and the source size has been intermediate between the possible extremes. By imposing all assumptions that minimize E^*, it is possible to lower our adopted values by 10–15 %; maximizing the acceptance procedure leads to a 20–25 % increase. The intermediate assumptions adpoted in this work yield maximum excitation energies up to $E^*/A\sim8$ MeV at the 1% probability level for the 2.4×10^6 events analyzed for the 8.0 GeV/c π^- + ^{197}Au system. This same prescription has been subsequently used for E^* and source Z_s and A_s determination for all the E900 and E900a hadron-induced reaction data [26].

ACKNOWLEDGMENTS

The authors thank R. N. Yoder, W. Lozowski, J. Vanderwerp, and T. Hall of Indiana University; and P. Pile, H. Brown, J. Scaduto, L. Toler, J. Bunce, J. Gould, R. Hackenberg, C. Woody, W. McGahern, F. Kobasiuk, and T. Mruczkowski from AGS for their assistance with the experiments. We are also grateful to A. Botvina and D. Durand for the use of their model calculations. This work was supported by the U.S. Department of Energy, the U.S. National Science Foundation, the National and Engineering Research Council of Canada, Grant No. P03B 048 15 of the Polish State Committee for Scientific Research, Indiana University Office of Research, the University Graduate School, Simon Fraser University, and the Robert A. Welch Foundation.

[1] G. Bertsch and P.J. Siemens, Phys. Lett. **126B**, 9 (1983).
[2] L.G. Moretto and G. Wozniak, Annu. Rev. Nucl. Sci. **43**, 379 (1993).
[3] J.P. Bondorf, A.S. Botvina, A.S. Iljinov, I.N. Mishustin, and K. Sneppen, Phys. Rep. **257**, 133 (1995).
[4] A. Botvina, A.S. Iljinov, and I.N. Mishustin, Nucl. Phys. **A507**, 649 (1990).
[5] W.A. Friedman, Phys. Rev. C **47**, 667 (1990).
[6] D.H.E. Gross, Rep. Prog. Phys. **53**, 605 (1990).
[7] J. Pochodzalla *et al.*, Phys. Rev. Lett. **75**, 1040 (1995).

[8] K. Kwiatkowski, D.S. Bracken, E. Renshaw Foxford, K.B. Morley, V.E. Viola, E.C. Pollacco, C. Volant, and R.G. Korteling, Phys. Lett. B **423**, 21 (1998).
[9] J.A. Hauger *et al.*, Phys. Rev. Lett. **77**, 235 (1996); J.A. Hauger *et al.*, Phys. Rev. C **62**, 024616 (2000).
[10] Y.G. Ma *et al.*, Phys. Lett. B **390**, 41 (1997).
[11] R. Wada *et al.* Phys. Rev. C **55**, 227 (1997).
[12] F. Goldenbaum *et al.*, Phys. Rev. Lett. **77**, 1230 (1996).
[13] D.H. Boal, C.K. Gelbke, and B.K. Jennings, Rev. Mod. Phys. **62**, 553 (1990).
[14] J. Albergo, S. Costa, E. Constanzo, and A. Rubbino, Nuovo Cimento Soc. Ital. Fis., A **89A**, 1 (1995).
[15] D. Durand, Nucl. Phys. **A541**, 266 (1992); code SIMON (in preparation).
[16] P. Danielewicz, Phys. Rev. C **51**, 716 (1995).
[17] K. Kwiatkowski, J. Bashkin, H. Karwowski, M. Fatyga, and V.E. Viola, Phys. Lett. B **171**, 41 (1986).
[18] D.S. Bracken, Ph.D. thesis, Indiana University, 1996.
[19] K. Kwiatkowski *et al.*, Nucl. Instrum. Methods Phys. Res. A **360**, 571 (1995).
[20] W.-c. Hsi *et al.*, Phys. Rev. Lett. **79**, 817 (1997).
[21] R.J. Charity *et al.*, Nucl. Phys. **A483**, 371 (1988).
[22] J. Galin and U. Jahnke, J. Phys. G **20**, 1105 (1994).
[23] P. Figuera *et al.*, Z. Phys. A **532**, 315 (1995).
[24] J.C. Steckmeyer *et al.*, Nucl. Phys. **A500**, 372 (1989); D. Cussol *et al.*, *ibid.* **A561**, 298 (1993).
[25] L. Beaulieu *et al.*, Phys. Rev. C **54**, R973 (1995).
[26] L. Beaulieu *et al.*, Phys. Rev. C **64**, 064604 (2001), following paper.
[27] K.B. Morley *et al.*, Phys. Rev. C **54**, 737 (1996).
[28] L.G. Moretto *et al.*, Nucl. Phys. **A247**, 211 (1975).
[29] W.-c. Hsi *et al.*, Phys. Rev. C **58**, R13 (1998).
[30] J.A. Hauger *et al.*, Phys. Rev. C **57**, 764 (1998); J. Lauret *et al.*, *ibid.* **57**, R1051 (1998).
[31] P. Danielewicz, S. Turbide, and L. Beaulieu (private communication).
[32] T. Egidy *et al.*, Eur. Phys. J. A **8**, 197 (2000).
[33] D. Polster *et al.*, Phys. Rev. C **51**, 1167 (1995).
[34] J. Toke *et al.*, Phys. Rev. Lett. **75**, 2920 (1995).
[35] A.S. Goldhaber, Phys. Rev. C **17**, 2243 (1978).
[36] R. Wada *et al.*, Phys. Rev. C **39**, 439 (1989).
[37] A. Botvina (private communication).
[38] L. Beaulieu *et al.*, Phys. Lett. B **463**, 159 (1999).
[39] T. Lefort *et al.*, Phys. Rev. Lett. **83**, 4033 (1999).